5-1-1997

The Probability Density Function of Ocean Surface Slopes and Its Effects on Radar Backscatter

Y. Liu
University of Southern Mississippi

XH Yan
University of Delaware

W.T. Liu
California Institute of Technology

P.A. Hwang
Stennis Space Center

The Probability Density Function of Ocean Surface Slopes and Its Effects on Radar Backscatter

Y. LIU

Institute of Marine Sciences, University of Southern Mississippi, Stennis Space Center, Mississippi

X.-H. YAN

Center for Remote Sensing, Graduate College of Marine Studies, University of Delaware, Newark, Delaware

W. T. LIU

Jet Propulsion Laboratory, California Institute of Technology, Pasadena, California

P. A. HWANG

Oceanography Division, Naval Research Laboratory, Stennis Space Center, Mississippi

(Manuscript received 5 September 1995, in final form 7 October 1996)

ABSTRACT

Based on Longuet-Higgins's theory of the probability distribution of wave amplitude and wave period and on some observations, a new probability density function (PDF) of ocean surface slopes is derived. It is

$$f(\zeta_x, \zeta_y) = \frac{n}{2\pi(n-1)\sigma_u\sigma_c} \times \left[1 + \frac{\zeta_x^2}{(n-1)\sigma_u^2} + \frac{\zeta_y^2}{(n-1)\sigma_c^2}\right]^{-(n+2)/2} + \text{skewness},$$

where ζ_x and ζ_y are the slope components in upwind and crosswind directions, respectively; σ_u^2 and σ_c^2 are the corresponding mean-square slopes.

The peakedness of slopes is generated by nonlinear wave–wave interactions in the range of gravity waves. The skewness of slopes is generated by nonlinear coupling between the short waves and the underlying long waves. The peakedness coefficient n of the detectable surface slopes is determined by both the spectral width of the gravity waves, and the ratio between the gravity wave mean-square slope and the detectable short wave mean-square slope. When n equals 10, the proposed PDF fits the Gram Charlier distribution, given by Cox and Munk, very well in the range of small slopes. When $n \to \infty$, it is very close to the Gaussian distribution.

Radar backscatter cross sections (RBCS), calculated from specular reflection theory using the new PDF of the C-band radar filtered surface slopes, are in keeping with empirically based *ERS-1* C-band scatterometer models. In other words, the proposed PDF can be used successfully in the specular reflection theory to predict the RBCS in the range of incidence angles away from normal incidence. This suggests that the proposed PDF can be used to describe the distribution of surface slopes over the full range of slopes. This is an improvement over the Gaussian distribution and the Gram Charlier distribution. The comparison between the calculated RBCS and the *ERS-1* C-band scatterometer models indicates that the peakedness coefficient n should be 5, for wind condition of $U_{10} \leq 10$ m s^{-1}. It is also found that the spectral width plays an important role on radar backscatter in the range of incidence angles less than 30°.

1. Introduction

The use of radar backscatter of a satellite scatterometer to determine the wind velocity at sea surface has been investigated extensively. When the incidence angle of radar beam is normal or nearly normal to the sea surface, the radar backscatter has generally been considered as specular (Barrick 1968; Valenzuela 1978; Donelan and Pierson 1987; Phillips 1988). Based on the geometrical optics approach, the specular reflection is proportional to the probability density function (PDF) of the sea surface slopes. The radar backscatter cross sections (RBCS) due to specular reflection (Barrick 1968; Valenzuela 1978; Apel 1987) are

$$\sigma_0(\theta) = \pi \sec^4\theta f(\zeta_x, \zeta_y)|R(0)|^2, \quad (1)$$

where θ is the radar incidence angle and $|R(0)|^2$ is the Fresnel reflection coefficient for normal incidence

Corresponding author address: Dr. Yuguang Liu, Institute of Marine Sciences, University of Southern Mississippi, Stennis Space Center, MS 39529.
E-mail: yuguang@sunfish.st.usm.edu

(Stewart 1985; Schanda 1976). In (1), the joint PDF of the surface slopes, $f(\zeta_x, \zeta_y)$, is evaluated at the specular points. Here ζ is the surface elevation; ζ_x and ζ_y are the slope components of the rough surface in two orthogonal directions at the specular points. To apply (1) to the ocean surface, one must keep in mind that only a portion of the total probability density is included in (1), that being the slopes contributed by ocean waves whose wavelengths are greater than the radar wavelength (Valenzuela 1978).

For an isotropically rough surface of Gaussian distribution, (1) becomes

$$\sigma_0(\theta) = \frac{|R(0)|^2}{s^2}\sec^4\theta \exp\left(-\frac{\tan^2\theta}{s^2}\right), \qquad (2)$$

where s^2 is the mean-square slope. Daley et al. (1973) and Barrick (1974) obtained relatively good agreement with measured cross sections at normal incidence ($\theta = 0$) when the mean-square slope measured by Cox and Munk (1954a,b) for a clean ocean surface was used. However, when the prediction using the same value of the parameter s^2 was extended to angles away from normal incidence ($\theta \neq 0$), one found considerable disagreement (Valenzuela 1978). This may imply that the slope distribution in the open ocean is not Gaussian.

In linear wave theory, both the surface elevations and the surface slopes are assumed to be Gaussian according to the central limit theorem of probability. For higher order approximation, both slope and elevation are found to obey the Gram Charlier distribution (Cox and Munk 1954a,b; Kinsman 1960, 1965; Huang and Long 1980) in the range of small slopes and elevations. Compared with the Gaussian distribution, the Gram Charlier distribution has two additional factors: peakedness and skewness. Theoretical results of Longuet-Higgins (1963) indicated that the skewness is due to the second-order nonlinear wave–wave interactions and the peakedness is due to the third-order nonlinear wave–wave interactions.

The Gram Charlier distribution replaces the Gaussian distribution for higher accuracy only in the range of small slopes and small elevations. In the range of large slopes and large elevations, both the Gaussian and Gram Charlier distributions fail to work. A weakness of the Gram Charlier distribution is that there is negative probability in the range of large slopes or large elevations. As indicated by Cox and Munk (1954a,b), the peakedness appears under very small slopes and very large slopes. The Gram Charlier distribution underestimates the peakedness of PDF in the range of very large slopes, but does not underestimate the skewness in the same range, thus causing a negative value of PDF. Therefore, the Gram Charlier distribution is also unsuitable to be used in the Eq. (1).

In this study, we try to derive a more satisfactory expression of PDF for the full range of wave slopes. If an appropriate joint PDF of slopes is obtained, one may expect it to bring Eq. (1) into agreement with backscatter measurements at angles away from normal incidence. In order to derive PDF of gravity wave slopes, we have to know the distributions of wave amplitude and wavelength. The distribution of wave amplitude derived by Longuet-Higgins (1975) is introduced in section 2a. The wave period distribution, based on the theory of Longuet-Higgins (1975) and some observations, is introduced in section 2b. The distribution of wavelength derived from the distribution of wave period is introduced in section 2c. The PDF of gravity wave slopes can be derived from the distributions of wave amplitude and wavelength using an assumption (sections 3a and 3b). The sea surface slopes, which can be detected by optical sensor or microwave radar, are the vector sum of the short wave slopes and the underlying long gravity wave slopes. Therefore, the PDF of detectable ocean surface slopes can be found from the gravity wave slope distribution and the short wave slope distribution (section 3c). Comparisons with field measurements of surface slopes (Cox and Munk 1954a,b) and *ERS-1* C-band scatterometer algorithms (CMOD3 and CMOD4) are given in section 4. The slope skewness is presented in section 5.

Generally, the sea surface waves can be defined as the motion of sea surface elevation with characteristic period, length, speed, and amplitude. The linear wave theory, which ignores nonlinear effects, models the sea surface elevation as the sum of many harmonics with unvariable frequencies and wavenumbers. Those harmonics, called as the component waves, cannot be seen directly but can be analyzed from wave records. In this paper, the slope, amplitude, period, and wavelength represent those of apparent waves. The apparent waves are the waves that can be seen directly by eyes or various sensors (camera, radar, and radio).

2. Distributions of wave amplitude, wave period, and wavelength of the surface gravity waves

a. Previous results

1) WAVE AMPLITUDE DISTRIBUTION

On the assumption that the sea surface is Gaussian and that the energy spectrum is sufficiently narrow, Longuet-Higgins (1975) derived two theoretical results on the probability distributions of wave amplitude and wave period.

The probability density of the wave amplitude a (defined as half the crest-to-trough wave height) is given by the well-known Rayleigh distribution

$$f(a) = \frac{a}{\mu_0}\exp\left(-\frac{a^2}{2\mu_0}\right), \qquad (3)$$

where μ_0 is the zeroth moment of the energy spectrum, which also corresponds to the mean-square surface amplitude.

The Rayleigh distribution of wave amplitude (3) was

confirmed by observation (Chakrabarti and Cooley 1977) in the open ocean and by experiment (Jacobson and Colonell 1972) in the laboratory. Liu and Housley (1968) found that the relationships among a few characteristic wave heights, obtained from laboratory, lake, and open ocean, are approximately equal to the theoretical results derived from Rayleigh distribution. This suggests that the distribution of wave amplitude is unrelated to the spectral width. Only in the case of very strong winds, Forristall (1978) found that the Weibull distribution fits data better than the Rayleigh distribution.

2) WAVE PERIOD DISTRIBUTION

The normalized probability density of the wave period derived by Longuet-Higgins (1975) under an assumption of narrow spectrum is

$$f(T_m) = \frac{\nu^2}{2[\nu^2 + (T_m - 1)^2]^{3/2}}, \tag{4}$$

where $T_m = \tau/\tau_m$ is the wave period normalized by the most-probable wave period, τ is the wave period (defined as the time interval between successive up-crossings of the mean level), and τ_m is the most-probable wave period. Originally τ_m was called the mean wave period by Longuet-Higgins because the most-probable period is almost equal to the mean wave period in the case of a narrow spectrum. The parameter ν represents the spectral width. The definition of ν is given by (7). The relationship between ν and another parameter of spectral width ϵ_s is

$$\nu \approx \frac{\epsilon_s}{2}, \tag{5}$$

where ϵ_s is defined as

$$\epsilon_s = \sqrt{\frac{m_0 m_4 - m_2^2}{m_0 m_4}}, \tag{6}$$

with the nth moment of the wave spectrum of surface elevation $S(\omega)$ defined as

$$m_n = \int S(\omega)\omega^n \, d\omega.$$

The value of the parameter ν can be also calculated by using the interquartile range of the wave period, $R_{\mathrm{IQ}}(\tau)$ (Longuet-Higgins 1975):

$$\nu = \frac{\sqrt{3}}{2} R_{\mathrm{IQ}}(\tau) = \frac{\sqrt{3}}{2}[Q_2 - Q_1], \tag{7}$$

where Q_2 and Q_1 are determined as

$$\frac{1}{4} = \int_{-\infty}^{Q_1} f(T_m)\, dT_m$$

$$\frac{3}{4} = \int_{-\infty}^{Q_2} f(T_m)\, dT_m. \tag{8}$$

The spectral width parameter ν, therefore, can also be calculated from the PDF of period.

Wider spectra can be found from ocean data. From wave data, Bretschneider (1959) and Davidan et al. (1973) found that the normalized PDF of wave period obeys the Weibull distribution

$$f(T_M) = \alpha j T_M^{j-1} e^{-\alpha T_M^j}, \tag{9}$$

where $T_M = \tau/\tau_M$ is the wave period normalized by the mean wave period τ_M. Bretschneider's result corresponds to the case where $j = 4$ and $\alpha = 0.675$. Davidan et al. later modified j from 4 to 3 and α from 0.675 to 0.712, based on different investigations. For comparison with a new form of wave period distribution introduced in the section 2b, the above results need to be expressed in the form normalized by the most-probable wave period τ_m. The relationship between τ_M and τ_m for the Weibull distribution (9) is

$$\tau_M^j = \frac{\alpha j}{j - 1}\tau_m^j, \tag{10}$$

which was obtained from

$$\frac{\partial f(\tau)}{\partial r}\Big|_{\tau=\tau_m} = 0$$

because the first-order derivative of the PDF is zero at the most-probable wave period τ_m. The PDF $f(T_m)$ can be obtained from $f(\tau)d\tau = f(T_M)dT_M = f(T_m)dT_m$, where $f(T_M)$ is from (9). Substituting (10) and the values of j and α, the results of Bretschneider and Davidan et al. can be expressed, respectively, as

$$f(T_m) = 3^{3/4}(4 \times 0.675)^{1/4} T_m^3 \exp\left(-\frac{3}{4}T_m^4\right), \tag{11}$$

and

$$f(T_m) = 2^{2/3}(3 \times 0.712)^{1/3} T_m^2 \exp\left(-\frac{2}{3}T_m^3\right). \tag{12}$$

b. A new form of wave period distribution

In order to derive the distribution of slopes, a new form of wave period PDF is needed for convenience in integral operation. The PDF of normalized wave period proposed here is

$$f(T_m) = \frac{(2n-1)^{n/2}}{\Gamma\left(\frac{n}{2}\right)2^{n-2}} T_m^{2n-1} \exp\left[-\frac{T_m^4(2n-1)}{4}\right], \tag{13}$$

where n is a new parameter related to the spectral width, and the Γ function is defined by (Abramowitz and Stegun 1972)

$$\Gamma(\alpha) = \int_0^\infty x^{\alpha-1}e^{-x}\, dx = 2\int_0^\infty y^{2\alpha-1}e^{-y^2}\, dy \tag{14}$$

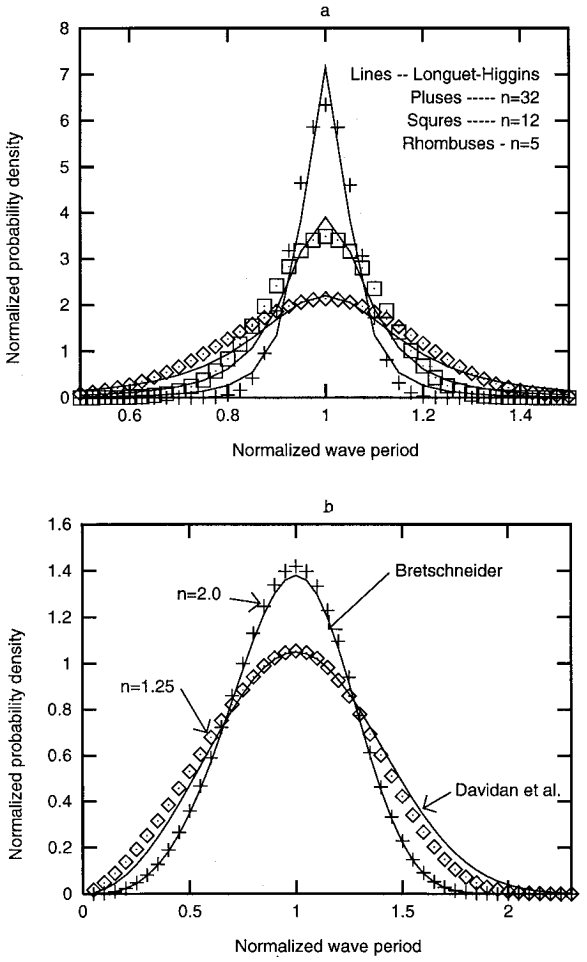

FIG. 1. The normalized PDF versus the normalized wave period. (a) Comparison with Longuet-Higgins's analytical solution. The solid lines are from Eq. (4), for $\nu = 0.07, 0.12, 0.18$ (top to bottom). The points are from Eq. (13), pluses for $n = 32$, squares for $n = 12$. (b) Comparison with field observations. The upper line is from Eq. (11), the lower line is from Eq. (12). The points are from Eq. (13), pluses for $n = 2.0$, diamonds for $n = 1.25$.

for $\alpha > 0$. In order to include the waves with sharp crests and shallow troughs, the wave period presented in (13) is defined as two times the time interval between successive crossings of the mean level. This definition can reflect the difference of wave periods between sharp crests and shallow troughs.

A comparison between (13) and Longuet-Higgins (1975) function (4) is given in Fig. 1a. Figure 1a shows that a good agreement between (13) and (4) is obtained, although there are obvious differences in the case of wider spectrum. Fortunately, in the case of wide spectrum, Eq. (13) with $n = 2.0$ fits the measurements of Bretschneider (1959) very well; and (13) with $n = 1.25$ fits the measurements of Davidan et al. (1973) very well, as shown in Fig. 1b. Therefore, (13) is an equivalent form of the theoretical result of Longuet-Higgins (1975), supplemented by the empirical results (11) and (12). Figure 1b reveals that the results of both Bretschneider and Davidan et al. are not in conflict with each other when the spectral width is considered. The result of Davidan et al. is suitable for a wide spectrum; the result of Bretschneider is suitable for a slightly narrower spectrum.

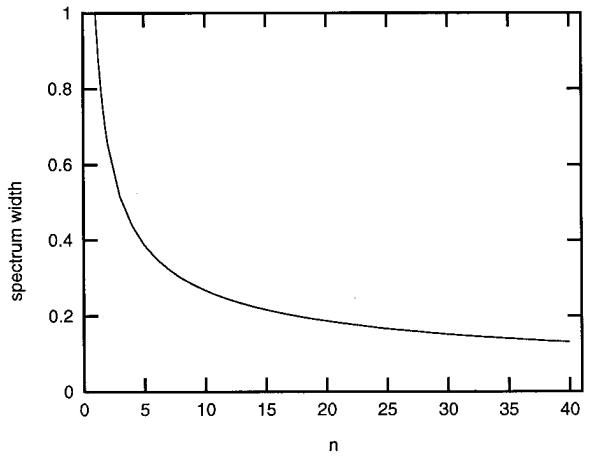

FIG. 2. The spectral width ϵ_s versus the spectral width related parameter n.

Following Longuet-Higgins (1975), we use (5) and (7) to calculate the spectral width parameter ϵ_s for the PDF (13). By doing so, the relationship between n and ϵ_s can be found. Figure 2 shows this relationship. The relationship shown in Fig. 2 is not very accurate and should be used only as a reference because Eq. (5) was derived by Longuet-Higgins (1975) under an assumption of narrow spectrum. An accurate relation can be obtained from (6) if the wave spectrum of surface elevation $S(\omega)$ is derived in advance. The derivation of $S(\omega)$ from the joint distributions of wave amplitude and wave period is very complicated (Bretschneider 1959, 1963).

c. Probability density function of wavelength

The dispersion relation for gravity waves in deep water is

$$\lambda = \frac{g}{2\pi}\tau^2 = \frac{g\tau_m^2}{2\pi}T_m^2, \tag{15}$$

where λ is the wavelength (defined as two times the space interval between successive crossings of the mean level). From (15) and (13), the PDF of wavelength λ can be derived as

$$f(\lambda) = \frac{2(n-1)^{n/2}}{\Gamma\left(\frac{n}{2}\right)2^{n/2}\lambda_m^n}\lambda^{n-1}\exp\left[-\frac{\lambda^2(n-1)}{2\lambda_m^2}\right], \tag{16}$$

where λ_m is the most-probable wavelength.

The dispersion relation (15) is approximately suitable for the apparent period τ and the apparent wavelength λ, according to the sea wave theory (Wen and Yu 1984). When $n = 2$, (16) corresponds to the Rayleigh distri-

bution, which was proposed by Bretschneider (1963) and Gluhovskii (1966) previously.

In the above derivation, a formula of probability theory on the distribution of the square of a random variable

$$f_{\varepsilon^2}(x) = \frac{1}{2\sqrt{x}}[f_\varepsilon(\sqrt{x}) + f_\varepsilon(-\sqrt{x})] \qquad (x > 0) \quad (17)$$

was used, where ε^2 is the square of random variable ε, x is the value of ε^2, and f_ε is the PDF of ε. Another formula on the basic property of PDF

$$\int_{-\infty}^{\infty} f(x)\, dx = 1 \quad (18)$$

was used to check the result.

3. Distribution of the ocean surface slope

a. An assumption of independence between wave height and wavelength

Bretschneider (1959, 1963) derived many spectral models of the gravity waves from the joint PDF of wave height and wave period. The one derived with the assumption of independence between wave height and wave period (or wavelength) appears to be most realistic and significant. The derived spectrum successfully predicted ''overshoot'' of the sea wave spectrum development, which was confirmed by many observations later. The form of the derived spectrum is the same as the P–M spectrum developed by Pierson and Moscowitz (1964) later from numerous observations. Therefore, Bretschneider's spectrum is still being used by marine engineers to this date.

The assumption of independence between wave height and wavelength is also based on many observations. For example, Krylov (1956) confirmed that for waves satisfying the condition of either $h \geq 0.2\bar{h}$ or $\tau \geq 0.4\bar{\tau}$ (where h and τ are the wave height and the wave period, respectively; overbar represents the mean value), the wave heights and the wave periods are approximately independent of each other. His figure also shows that the probability satisfying the above condition is 95%. Based on numerous measurements, Gluhovskii (1966) proposed a semiempirical joint PDF of wave height and wave period; he also confirmed that wave height and wave period are statistically independent.

Wave height and wave period are approximately independent of each other for either wind waves or swells, but not for mixed waves. From mixed wave records, Gooda (1977) found that there is a strong correlation between wave height and wave period. In fact, the correlation is mainly caused by the two or more groups of notable waves with different characteristic wave heights and periods in the mixed waves.

b. Distribution of the gravity wave slope

At first, let us investigate the distribution of the gravity wave slopes for simple wind waves or swells. Generally, slope is defined by

$$r = \sqrt{\zeta_x^2 + \zeta_y^2} = ak|\cos\phi| = \frac{2\pi a}{\lambda}|\cos\phi|, \quad (19)$$

where k is the wavenumber and ϕ is the phase angle. The corresponding averaged slope in a wave period is

$$\bar{r} = \frac{1}{2\pi}\int_0^{2\pi} r\, d\phi = \frac{a}{\lambda/4}. \quad (20)$$

On the assumption that wave amplitude and wave period (or wavelength) are independent of each other, the probability density of averaged wave slope can be derived from (20), (3), and (16). It is

$$f(r) = \frac{n}{(n-1)}\frac{r}{\sigma^2}\left[1 + \frac{r^2}{(n-1)\sigma^2}\right]^{-(n+2)/2}, \quad (21)$$

where σ^2 is a parameter related to the mean-square slope. In the derivation, a formula of probability theory on the distribution of quotient was used:

$$f_{\varepsilon_1/\varepsilon_2}(x) = \int_{-\infty}^{\infty} f_{\varepsilon_1}(x_2 x)\, f_{\varepsilon_2}(x_2)|x_2|\, dx_2, \quad (22)$$

where ε_1 and ε_2 are two independent random variables, and x is the value of $\varepsilon_1/\varepsilon_2$.

If we assume that ϕ in (19) obeys uniform distribution in an interval between 0 and 2π, the slope defined by (19) can be confirmed to obey the same distribution as the averaged slope by using numerical integration. The method using numerical integration is similar to that of (29) introduced later. So, (21) is considered as the distribution of gravity wave slope.

The joint PDF of the two components of slope for the isotropic surface derived from (21) is

$$f(\zeta_x, \zeta_y) = \frac{n}{2\pi(n-1)\sigma^2}\left[1 + \frac{\zeta_x^2 + \zeta_y^2}{(n-1)\sigma^2}\right]^{-(n+2)/2}. \quad (23)$$

The proof of (23) is shown in appendix A. Equation (23) is suitable for an isotropic rough surface, but not nonisotropic real surface. An empirical extension of (23) for nonisotropic surface is

$$f(\zeta_x, \zeta_y) = \frac{n}{2\pi(n-1)\sigma_u\sigma_c} \times \left[1 + \frac{\zeta_x^2}{(n-1)\sigma_u^2} + \frac{\zeta_y^2}{(n-1)\sigma_c^2}\right]^{-(n+2)/2}, \quad (24)$$

where σ_u^2 and σ_c^2 are the mean-square slopes in the upwind direction and crosswind direction, respectively. The corresponding normalized form is

$$f(X, Y) = \frac{n}{2\pi(n-1)} \times \left[1 + \frac{X^2}{(n-1)} + \frac{Y^2}{(n-1)}\right]^{-(n+2)/2}, \quad (25)$$

where $X = \zeta_x/\sigma_u$, $Y = \zeta_y/\sigma_c$.

The variances of the distribution, σ_x^2, σ_y^2, can be calculated from (24). They are

$$\sigma_x^2 = \int_{-\infty}^{\infty}\int_{-\infty}^{\infty} \zeta_x^2 f(\zeta_x, \zeta_y)\, d\zeta_x\, d\zeta_y = \frac{n-1}{n-2}\sigma_u^2,$$

$$\sigma_y^2 = \int_{-\infty}^{\infty}\int_{-\infty}^{\infty} \zeta_y^2 f(\zeta_x, \zeta_y)\, d\zeta_x\, d\zeta_y = \frac{n-1}{n-2}\sigma_c^2. \quad (26)$$

Equation (26) shows that the variances of slope distribution, σ_x^2 and σ_y^2, depend on the spectral width related parameter n. When $n \to \infty$, they approach σ_u^2 and σ_c^2, respectively. Physically, σ_u^2 and σ_c^2, named ''mean-square slopes,'' represent the slope variances without consideration of nonlinear wave–wave interaction. The differences between the two types of ''variances'' represent the gain of slope variances generated by nonlinear wave–wave interactions.

Figures 3a and 3b show the comparison of $f(X, 0)$, or $f(0, Y)$, given by (25), with the Gaussian distribution in different slope ranges. Figure 3a shows that there is a peak of slope distribution near zero slope. Obviously, the peakedness of slope distribution is controlled by the value of n, so n is called the peakedness coefficient. In fact, the value of n is approximately inverse to both the peakedness of slope distribution and the spectral width. Figure 3b shows the proposed PDF with very large values of n is close to the Gaussian distribution. This means that the slopes, generated by the gravity waves with very narrow spectral width, obey a Gaussian distribution. The proposed PDF with $n = 5$ has much higher values than the Gaussian distribution in the range of large slopes.

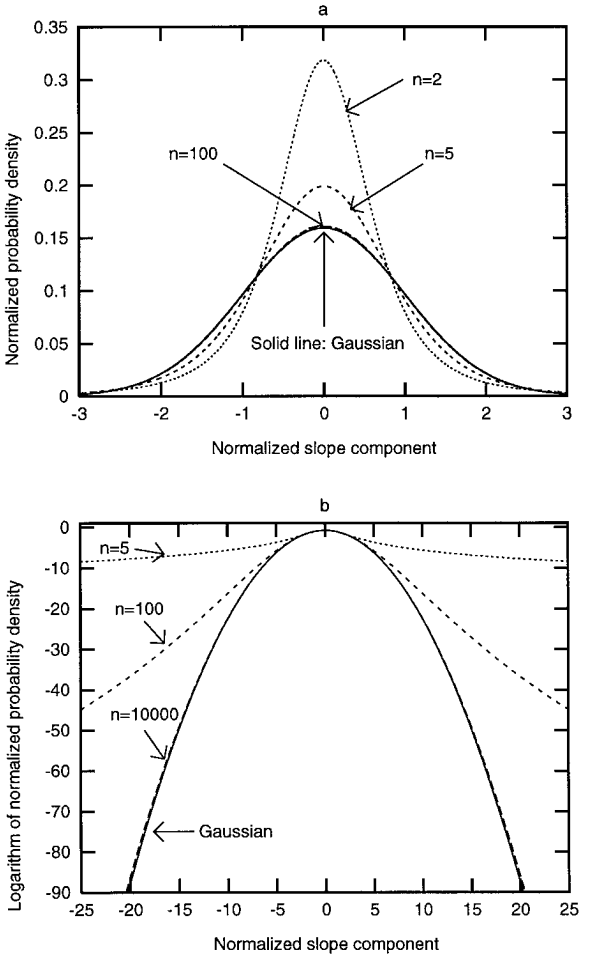

FIG. 3. The normalized joint PDF $f(X, 0)$ or $f(0, Y)$ versus the normalized slope component, either X or Y. Solid line represents the Gaussian distribution; broken lines represent the PDF (25) with different values of n marked on the curves. (a) A comparison in the range of small slopes. (b) A comparison in a very wide range where the PDF is expressed by common logarithm.

c. Distribution of the detectable ocean surface slope

For convenience, we call the ocean surface slopes, generated by both the long gravity waves and the short gravity–capillary waves riding on them, the detectable slopes. The detectable slopes on the ocean surface can be described by

$$\boldsymbol{\zeta}(k) = \boldsymbol{\zeta}_1 + \boldsymbol{\zeta}_2(k), \quad (27)$$

where $\boldsymbol{\zeta}_1$ is the slope of gravity waves, $\boldsymbol{\zeta}_2$ is the slope of short gravity–capillary waves riding on longer gravity waves; k is the wavenumber, which is used here because sometimes we are concerned about the slopes up to k. Of course, optical sensors can detect all the slopes generated by water waves, but microwave radars can only detect a part of the slopes up to the radar frequency (Valenzuela 1978; Brown 1990; Jackson et al. 1992). In the later case, the slopes measured by radar are also called filtered slopes (Jackson et al. 1992). According to Liu and Yan (1995), the interactions among the wind drift, the short waves, and the underlying long waves may cause the short wave to break under the condition of strong winds. If we ignore the influence on slope distribution function from the above interactions, the two parts of the water waves can be assumed to be independent of each other, and the distribution of the detectable slopes can be expressed by

$$f(X, Y) = \sigma_u\sigma_c f(\zeta_x, \zeta_y), \quad (28)$$

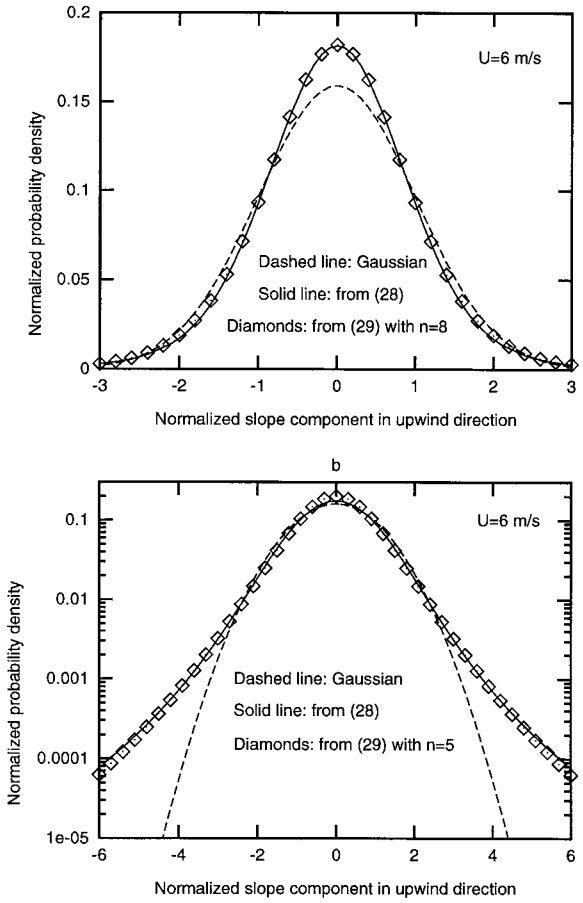

FIG. 4. Examples showing the comparison of Eq. (29) with Eq. (28).

with

$$f(\zeta_x, \zeta_y) = \int_{-\infty}^{\infty}\int_{-\infty}^{\infty} f_1(\zeta_{x1}, \zeta_{y1}) f_2(\zeta_x - \zeta_{x1}, \zeta_y - \zeta_{y1})\, d\zeta_{x1}\, d\zeta_{y1},$$

where $f(\zeta_x, \zeta_y)$, $f_1(\zeta_{x1}, \zeta_{y1})$, and $f_2(\zeta_{x2}, \zeta_{y2})$ are the joint PDF of the slope $\boldsymbol{\zeta}$, $\boldsymbol{\zeta}_1$, and $\boldsymbol{\zeta}_2$, respectively. The gravity wave slope PDF $f_1(\zeta_{x1}, \zeta_{y1})$ is given by (24). The short wave slopes can be assumed to obey the Gaussian distribution, which is accepted generally.

Because of the complexity, we cannot obtain a closed form solution for (28). But the results of numerical integrations of (28) confirm that $f(x, y)$ in (28) can be described by the same function as $f_1(\zeta_{x1}, \zeta_{y1})$, except with different peakedness coefficients. So, the normalized form of detectable surface slope distribution, which has the same form as (25), can be expressed by

$$f(X, Y) = \frac{n}{2\pi(n-1)}\left[1 + \frac{X^2}{(n-1)} + \frac{Y^2}{(n-1)}\right]^{-(n+2)/2}, \quad (29)$$

with

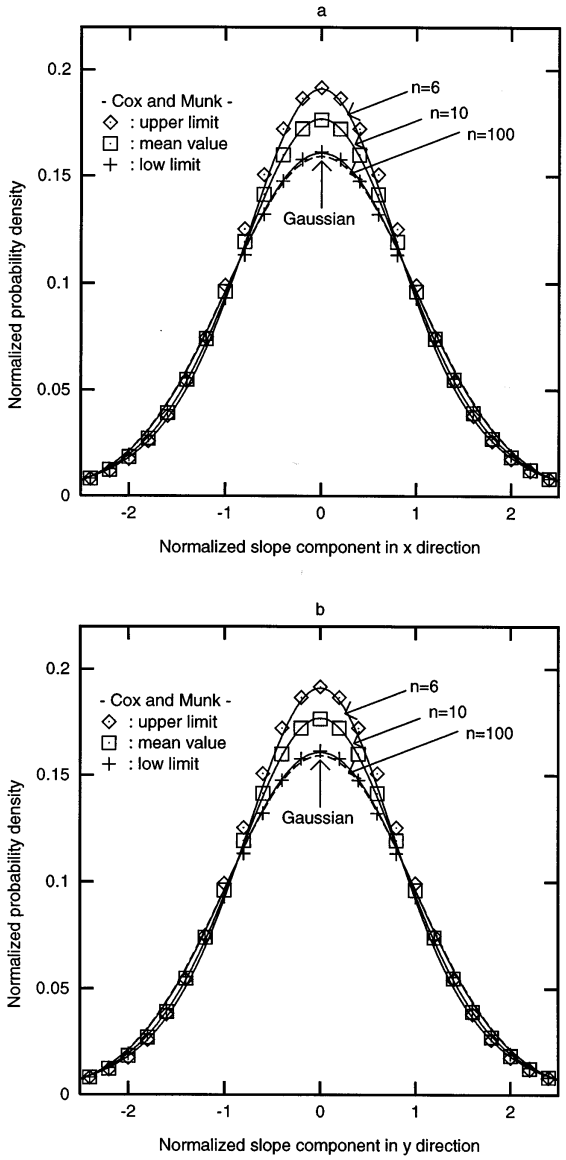

FIG. 5. Comparison of the proposed PDF (29) with the Gram Charlier distribution (30). (a) The normalized joint probability density $f(X, 0)$ versus the normalized slope component X. (b) The $f(0, Y)$ versus Y.

$$n = \begin{cases} f'\left(\dfrac{\sigma_{2u}}{\sigma_{1u}}, \dfrac{\sigma_{2c}}{\sigma_{1c}}, n_g\right) & \text{for the range of } X < 3 \text{ and } Y < 3 \\ f''\left(\dfrac{\sigma_{2u}}{\sigma_{1u}}, \dfrac{\sigma_{2c}}{\sigma_{1c}}, n_g\right) & \text{for } 1 < X < 6 \text{ and } 1 < Y < 6, \end{cases}$$

where n_g is the peakedness coefficient of the gravity wave slope, and f' and f'' are two different unknown functions. The value of n is determined by comparing (28) with (29). The maximum relative error between (29) and (28) would be less than 5%, if the value of n is selected suitably. Two examples with wind speed of 6 m s^{-1} are shown in Figs. 4a and 4b. In Fig. 4, the

dashed line represents the Gaussian distribution, which is generally accepted now. The diamonds represent $f(X, 0)$ in (29) with $n = 8$ in Fig. 4a and $n = 5$ in Fig. 4b, respectively. The solid line represents $f(X, 0)$ calculated from (28). The mean-square slopes used in (28) are calculated from the empirical formulas in appendix B. In the calculation of mean-square slopes, the maximum wavenumber of the detectable wave slopes is selected to be 1250 rad m^{-1} for Fig. 4a and 111 rad m^{-1} for Fig. 4b, respectively. The peakedness coefficient of the gravity wave slopes n_g is elected to be 2.0 for Fig. 4a and 3.6 for Fig. 4b, respectively. Figure 4a is suitable in the range of small slopes ($|X| < 3$), and Fig. 4b is suitable in the range of larger slopes ($1 < |X| < 6$). For the range of small slopes, the selection of n_g is based on the measurements of the wave period distribution of Bretschneider (1959) and Gluhovskii (1966). For the range of large slopes, the selection of n_g is based on the best fit of the calculated RBCS with *ERS-1* C-band scatterometer models. As observed by Cox and Munk (1954a,b), the skewness of surface slopes almost disappears for a slick surface, but the peakedness is almost the same as for a clean surface. This suggests that the slope peakedness is generated by nonlinear wave–wave interactions within the range of gravity waves. Similar to the skewness of surface elevation discussed by Phillips (1977), the peakedness of surface slope distribution appears to be a statistical consequence of the tendency of the waves to form sharp crests and shallow troughs.

4. Comparison with measurements

a. Comparison with measurements of Cox and Munk

Cox and Munk (1954a,b) found that their observed slopes can be described by the Gram Charlier distribution:

$$f(\zeta_x, \zeta_y) = \frac{1}{2\pi\sigma_u\sigma_c} e^{-(X^2+Y^2)/2} \times \left[1 - \frac{1}{2}c_{21}(Y^2 - 1)X - \frac{1}{6}c_{03}(X^3 - 3X) + \frac{1}{24}c_{40}(Y^4 - 6Y^2 + 3) + \frac{1}{4}c_{22}(Y^2 - 1) \times (X^2 - 1) + \frac{1}{24}c_{04}(X^4 - 6X^2 + 3)\right] \quad (30)$$

for slopes up to $X = Y = 2.5$. The skewness coefficients c_{21} and c_{03} for clean water are

$$c_{21} = (0.01 - 0.0088U_{10}) \pm 0.03,$$
$$c_{03} = (0.04 - 0.034U_{10}) \pm 0.12, \quad (31)$$

where the influence of c_{21} is much less than that of c_{03}. The peakedness coefficients c_{40}, c_{22}, and c_{04} for clean water are

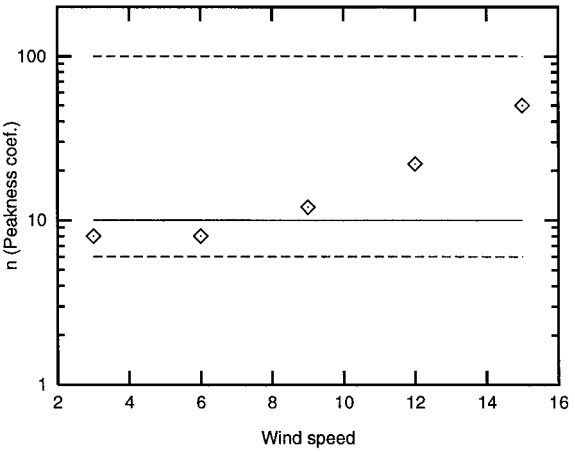

FIG. 6. The peakedness coefficient n of the slopes detectable by the optical sensor, in the range of small slopes ($X < 2.5$, $Y < 2.5$), plotted as a function of wind speed.

$$c_{40} = 0.40 \pm 0.23, \quad c_{22} = 0.12 \pm 0.06,$$
$$c_{04} = 0.23 \pm 0.41. \quad (32)$$

The values following "±" represent one standard deviation of the derived values from the best-fit regression curves.

Figure 5a shows the comparison of upwind component, $f(X, 0)$, given by (29) and the Gram Charlier distribution given by (30), when the skewness is excluded. Figure 5b shows the comparison of the crosswind component, $f(0, Y)$, given by (29) and the Gram Charlier distribution given by (30). Figures 5a and 5b show that the Gram Charlier distribution with an upper limit of the peakedness corresponding to a positive sign in (31) can be fitted by (29) with $n = 6$; and the Gram Charlier distribution with a low limit of the peakedness corresponding to a negative sign in (31) can be fitted by (29) with $n = 100$. The Gram Charlier distribution with a mean peakedness given by (31) can be fitted by (29) with $n = 10$.

Following the example in Fig. 4a, the peakedness coefficients of the surface slopes detectable with optical sensor, calculated from (28), are found to vary from 8 to 50, when the wind speed varies from 3 m s^{-1} to 15 m s^{-1} and when the peakedness coefficient of the gravity wave slopes n_g is selected to be 2.0. The peakedness of the detectable surface slopes is controlled by the ratio between the mean-square slope of the gravity waves and that of the short gravity–capillary waves. For optical sensor, the mean-square slope of the detectable short gravity–capillary waves is larger than that of the gravity waves (Liu and Yan 1995; Hwang et al. 1996). For C-band radar, the reverse is true. The peakedness coefficients calculated from (28) as a function of wind speed are shown in Fig. 6 as diamonds. In Fig. 6, solid line ($n = 10$), upper dashed line ($n = 100$), and lower dashed line ($n = 6$) represent the mean value and the range of one standard deviation observed by Cox and Munk (1954a,b), respectively.

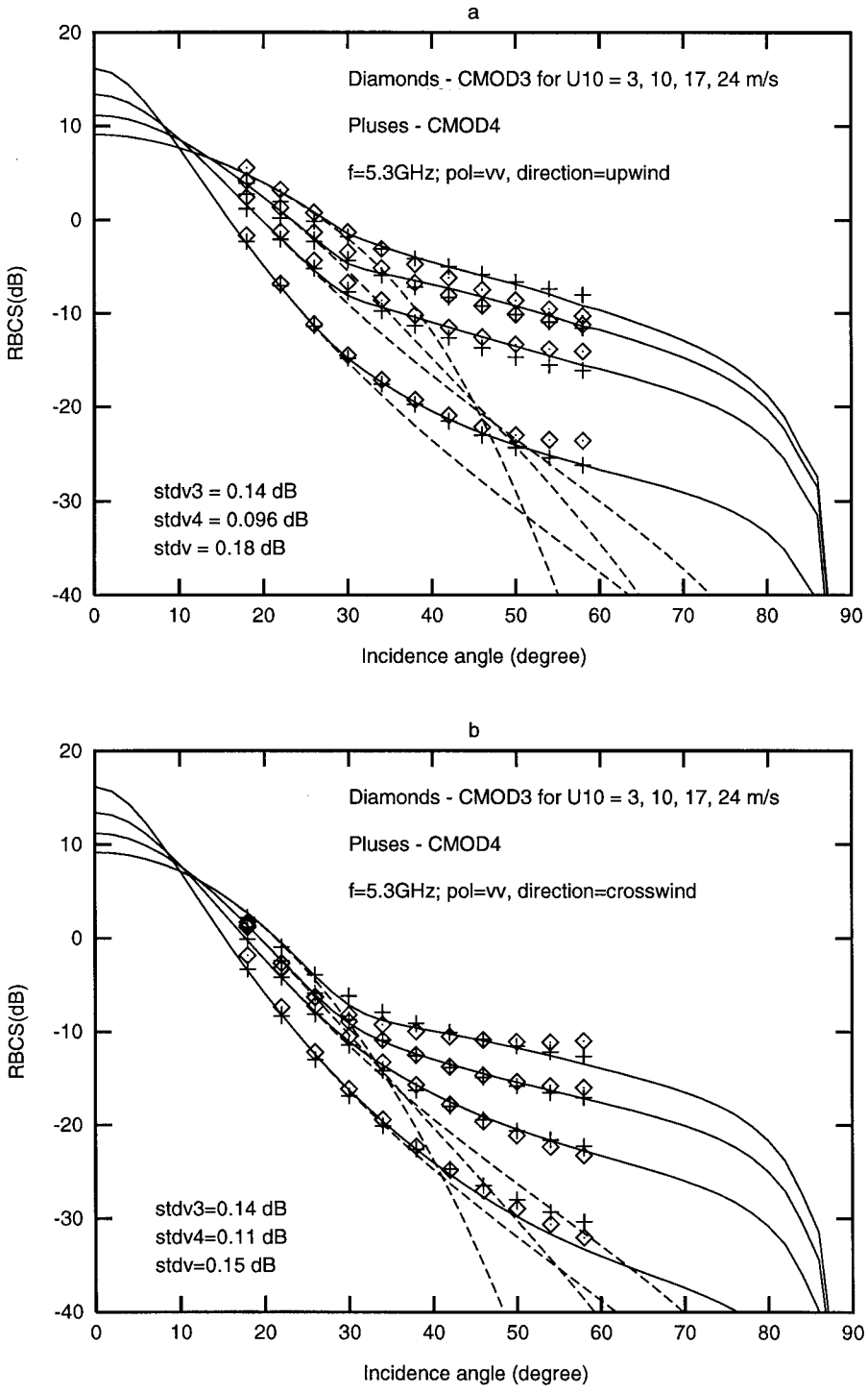

FIG. 7. The radar backscatter cross sections (RBCS in dB) for vertically polarized 5.3-GHz radar as a function of incidence angle with wind speed as a parameter. The solid lines represent the calculated RBCS due to both Bragg resonance and specular reflection by using the proposed PDF (29). The dashed lines represent the calculated RBCS due to specular reflection only. (a) Upwind direction. (b) Crosswind direction. (c) Downwind direction.

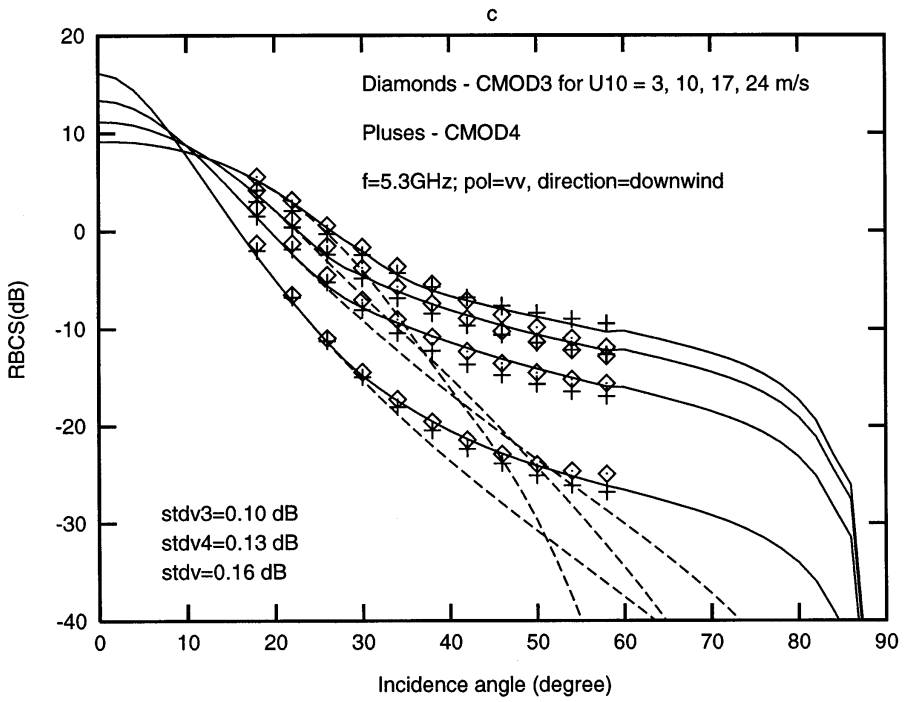

FIG. 7. (*Continued*)

b. Comparison with C-band empirical models

A comparison with the *ERS-1* scatterometer wind recovery algorithms involves radar backscatter theory. A model of the radar backscatter due to both specular reflection and Bragg resonance (Barrick 1968; Wright 1968; Valenzuela 1978; Stewart 1985; Donelan and Pierson 1987; Apel 1994; Liu and Pierson 1994; Liu and Yan 1995) is

$$\sigma_0 = \sigma_0^R + \sigma_0^B, \tag{33}$$

where σ_0^R is the RBCS due to specular reflection and σ_0^B is the RBCS due to Bragg resonance. This model does not include the contributions due to white caps, wedges, and jumps, although they are important in some cases (Donelan and Pierson 1987; Phillips 1988; Trizna et al. 1993; Wetzel 1993; Lee et al. 1995). The σ_0^B is calculated from the two-scale model of Bragg resonance (Wright 1968; Stewart 1985). The mean-square slopes, used in this study, are from appendix B. The criterion on length scale separating the reflection and the diffraction is: the reflection takes place only for those sea surface waves with wavelengths larger than radar wavelength (Valenzuela 1978), the diffraction exists only for the other waves. It should be noted that many different criterions are used by different authors, because of the requirement of best fit of theoretical RBCS, calculated from different models of mean-square slopes, slope PDF and short wave spectrum, with radar measurements.

The scatterometer in *ERS-1* is an active radar at C-band of 5.3 GHz and vertical polarization. An empirically based wind recovery algorithm, CMOD3, was originated from the European Center for Medium-Range Weather Forecasts (ECMWF) and has been in use in all stations of the European Space Agency (ESA) since 10 July 1992. CMOD4 is another ESA operational algorithm developed at ECMWF. These current models were obtained from many field measurements (Hoffman 1993; Anderson et al. 1991a,b). The CMOD3 formulas, used in this paper, were taken from Guignard (1992, personal communication), and the formulas for CMOD4 were provided by S. R. Dunbar (1995, personal communication).

Figure 7 gives a comparison of the radar backscatter cross sections (RBCS in dB), calculated from the radar backscatter theory by using the proposed PDF (29), with the empirical models CMOD3 and CMOD4. Figure 7a is for the upwind direction, Fig. 7b is for the crosswind direction, and Fig. 7c is for the downwind direction. In Fig. 7, ''stdv'' represents the standard deviation between CMOD3 and CMOD4; ''stdv3'' represents the standard deviation between the calculated RBCS and CMOD3; ''stdv4'' represents the standard deviation between the calculated RBCS and CMOD4. The agreement between the theoretical RBCS calculated by using proposed PDF of slopes and the empirical models (CMOD3 and CMOD4) is excellent. Figure 7 also shows that the specular reflection (shown as dashed curves) plays a significant role only for incidence angles less than about 30°. The value of the peakedness coefficient n in (29) is selected to be 5 for $U_{10} = 3$ m s^{-1} and 10 m/s, 8 for $U_{10} = 17$ m s^{-1}, and 25 for $U_{10} = 24$ m s^{-1}.

An example of the sensitivity of the peakedness coefficient n in the radar backscatter computation is shown

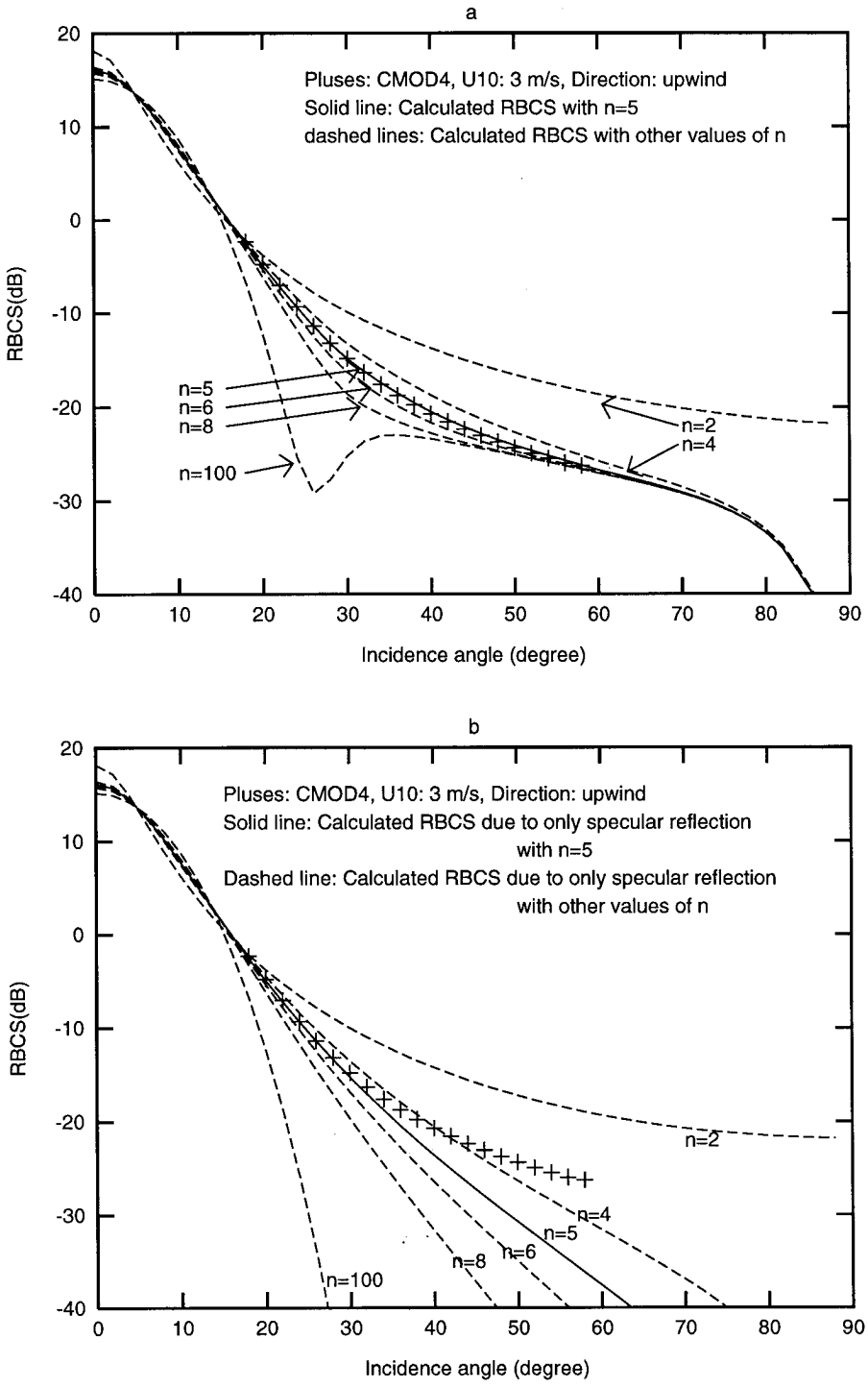

FIG. 8. The radar backscatter cross sections (RBCS in dB) for vertically polarized 5.3-GHz radar as a function of incidence. (a) Sensitivity test of the peakedness coefficient *n*. The lines represent the calculated RBCS due to both Bragg resonance and specular reflection with different values of *n* shown on the curves. (b) Same as (a) but the lines represent calculated RBCS due to only specular reflection.

in Fig. 8. Figure 8a gives a comparison of the theoretical RBCS with the empirical model CMOD4 for $U_{10} = 3$ m/s. The best fit obviously occurs near $n = 5$ for this wind speed. The comparison of the calculated RBCS due to only specular reflection with the empirical model CMOD4 is shown in Fig. 8b and further illustrates that the specular reflection is significant in the range of incidence angles less than 30°. From empirical fitting with the CMOD3 and CMOD4, the proposed values of the peakedness coefficient n as a function of wind speed is shown in Fig. 9 as a solid line.

5. Skewness of surface slopes

Based on the form of theoretical formula of Longuet-Higgins (1963), the measurements of Cox and Munk (1954a,b) and the empirical algorithms of C-band scatterometer, an empirical formula of slope skewness is here suggested as

$$f_{\rm sk}(\zeta_x, \zeta_y) = \frac{1}{2\pi\sigma_u\sigma_c}\exp\left[-\left(\frac{\zeta_x^2}{2\sigma_u^2} + \frac{\zeta_y^2}{2\sigma_c^2}\right)\right]\frac{1}{6}\lambda_{\rm sk}\cos\phi\left[\left(\frac{\zeta_x^2}{\sigma_u^2} + \frac{\zeta_y^2}{\sigma_c^2}\right)^{3/2} - 3\left(\frac{\zeta_x^2}{\sigma_u^2} + \frac{\zeta_y^2}{\sigma_c^2}\right)^{1/2}\right], \tag{34}$$

where ϕ is the wind direction and $\lambda_{\rm sk}$ is the skewness coefficient. Combining (29) and (34), the joint PDF of surface slopes including both peakedness and skewness is

$$f(\zeta_x, \zeta_y) = \frac{n}{2\pi(n-1)\sigma_{\zeta_x}\sigma_{\zeta_y}} \times \left[1 + \frac{\zeta_x^2}{(n-1)\sigma_{\zeta_x}^2} + \frac{\zeta_y^2}{(n-1)\sigma_{\zeta_y}^2}\right]^{-(n+2)/2} - f_{\rm sk}(\zeta_x, \zeta_y). \tag{35}$$

The proposed PDF including skewness in the upwind direction, expressed by (35), is compared with the Gram Charlier distribution measured by Cox and Munk (1954a,b) in Fig. 10, which shows that the two slope distributions are almost the same at low and middle winds. In Fig. 10, the upper group of data is for $U = 5$ m s^{-1} and the lower group is for $U = 10$ m s^{-1}. The solid lines represent the proposed PDF (35) with skewness (34). The dashed lines represent the Gaussian distribution. The discrete symbols, pluses and diamonds, represent the Gram Charlier distribution measured by Cox and Munk (1954a,b) for $U = 5$ m s^{-1} and $u = 10$ m s^{-1}, respectively. The middle pluses and the middle diamonds in all groups correspond to the mean values of the peakedness coefficients (32) and the skewness coefficients (31). The pluses and the diamonds of two sides in all groups correspond to the upper or the lower limit of the peakedness coefficients and the skewness coefficients. The values of σ_u and σ_c are from Cox and Monk (1954a,b).

Cox and Munk (1954a,b) found that the skewness of wave slopes almost disappears for a slick surface, but the peakedness coefficients are almost the same as for a clean surface. This suggests that the skewness is caused by the coupling between the short waves and the underlying long waves. For slick surfaces, this coupling reduces significantly because of the dumping of short waves. The slick surface has no sufficient surface tension to retain the short waves. In the absence of short waves, the coupling vanishes. In consideration of both the observation by Cox and Munk (1954a,b) and the theory of Longuet-Higgins (1963), we conclude that the skewness is generated by nonlinear wave–wave interaction between the short waves and the underlying long waves.

The skewness coefficient of Cox and Munk (1954a,b) or Longuet-Higgins (1982) is obtained based on the measurements of Cox and Munk (1954a,b). So it is correct only in the range of small slopes ($X < 2.5$ and $Y < 2.5$) for winds less than 14 m/s and for unfiltered waves. For *ERS-1* C-band radar filtered slopes and for the range of large slopes ($1 < X < 6$ and $1 < Y < 6$), the value of skewness coefficient should be different from the above case. Based on the best fit of the calculated RBCS with *ERS-1* empirical models, the skewness coefficient is given as follows: $\lambda_{\rm sk} = -0.001$ when $U_{10} = 3$ m s^{-1}; $\lambda_{\rm sk} = -0.025$ when $U_{10} = 10$ m s^{-1}; $\lambda_{\rm sk} = -0.070$ when $U_{10} = 17$ m s^{-1}; $\lambda_{\rm sk} = -0.150$ when $U_{10} = 24$ m s^{-1}. Because of the small order, this should be carefully investigated after a more accurate expression of the mean-square slope and a more complete model of radar backscatter are given. The present study on the skewness in this paper is insufficient.

Figure 11 gives a comparison between the radar backscatter cross sections (RBCS in dB), calculated from the radar backscatter theory by using the proposed PDF (35) with the skewness (34), with the RBCS obtained from *ERS-1* empirical models at an incidence angle of 25°. Dashed lines represent the calculated RBCS due to specular reflection only. Solid lines represent the calculated RBCS due to both Bragg resonance and specular reflection. This figure reveals that the order of the skewness is reasonable. A comparison of theoretical RBCS predicted by using the proposed PDF, Gaussian distribution, and Gram Charlier distribution is given in appendix C. This comparison shows that the proposed PDF is an improvement over both the Gaussian distribution and the Gram Charlier distribution.

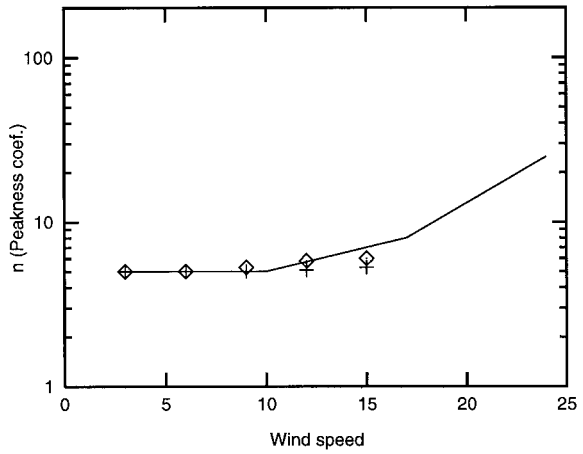

FIG. 9. The peakedness coefficient of the slopes filtered by the C-band radar, in the range of large slopes ($1 < \eta < 6$), versus the wind speed: Diamonds represent the values suitable to fit (28) in the upwind direction, pluses represent the values suitable to fit (28) in the crosswind direction, solid line represents the values suitable to fit *ERS-1* radar backscatter models.

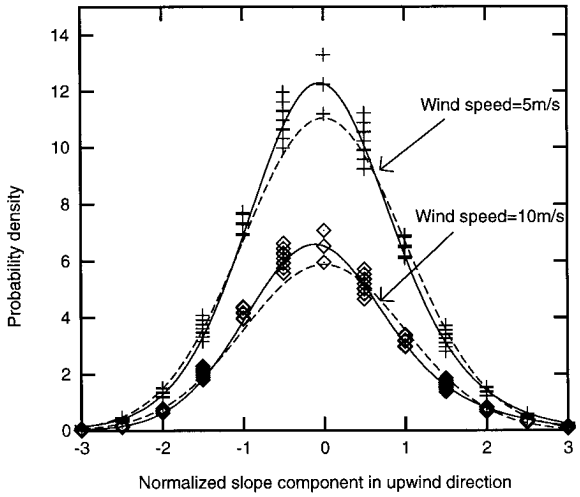

FIG. 10. The PDF $f(x, 0)$ in the upwind direction versus the normalized wave slope component X—a comparison between the proposed PDF and the Gram Charlier distribution measured by Cox and Munk.

6. Summary

On the assumption that the sea surface is Gaussian and that the energy spectrum is sufficiently narrow, Longuet-Higgins (1975) derived theoretical results of the PDF of wave magnitude and wave period. An equivalent form of the PDF of wave period is here obtained based on the theoretical result of Longuet-Higgins (1975) and the observations of Bretschneider (1959) and Davidan et al. (1973). The PDF of wavelength is derived from the equivalent form of wave period distribution by using the dispersion relation of gravity waves in deep water. With an additional assumption that wave period and wave amplitude are independent of each other, the PDF of the gravity wave slopes is also derived. The assumption of independence between wave period and wave amplitude is in general agreement with field observations (Krylov 1956; Bretschneider 1963; Gluhovskii 1966). Deviation from this assumption will increase the probability density in the range of large slopes. The deviation can be counteracted by adjusting the peakedness coefficient n. The detectable surface slope is the vector sum of the short wave slope and the underlying long wave slope. The PDF of the detectable surface slopes has been confirmed to be the same as the gravity wave slope distribution but with different values of the peakedness coefficient.

The most important character of the proposed PDF is that it is related to spectral width. The wider the spectrum, the larger the peakedness. A spectral width related parameter n is used to describe the peakedness. When $n \to \infty$, a very narrow spectrum results and the proposed PDF is just the Gaussian distribution. The peakedness of the gravity wave slopes is considered to be generated by the nonlinear wave–wave interactions in the range of gravity waves. When $n = 10$, the proposed PDF agrees with the Gram Charlier distribution of Cox and Munk (1954a,b) in the range of small slopes. The Gram Charlier distribution works well in the range of small slopes, but it does not work in the range of large slopes. The proposed PDF is an improvement over the Gram Charlier distribution. It works well in the full range of surface slopes, hence it can be used to predict the RBCS in the incidence angles away from normal incidence. The radar backscatter values predicted by this PDF of surface slope in the range of large slopes fit the empirical models of *ERS-1* scatterometer wind recovery

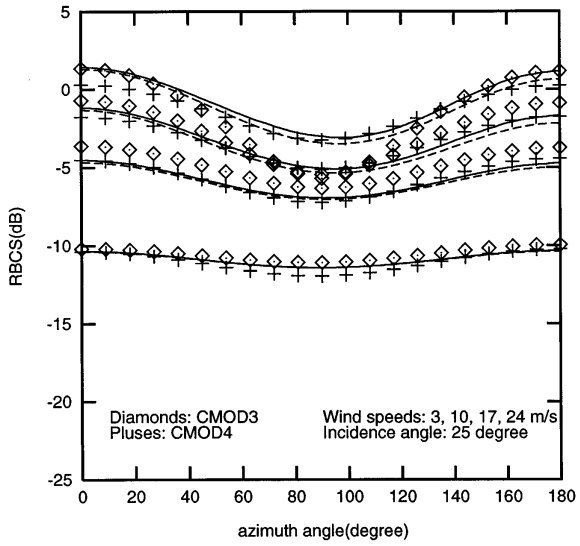

FIG. 11. Calculated and measured radar backscatter cross sections (RBCS in dB) for vertically polarized 5.3-GHz radar at an incidence angle of 25° as a function of azimuth angle, with wind speed as a parameter. The measured RBCS are from CMOD3 and CMOD4. The solid lines represent the RBCS calculated from radar backscatter theory by using the proposed PDF (35). The dashed lines represent the RBCS due to the specular reflection only.

algorithms very well. Therefore, the derived result is proposed for use as the PDF (probability density function) of the tangent-plane slopes (Valenzuela 1978) in the specular reflection theory (Barrick 1968).

Acknowledgments. We are very grateful to Professors Owen M. Phillips, Willard J. Pierson Jr., and Zhouwen Yu for their valuable advice. We thank Dr. Richard T. Field and Prof. Kuo-Chuin Wong for their help in the manuscript modification and Dr. Scott R. Dunbar for kindly providing *ERS-1* CMOD4 Fortran subroutine. We also thank the anonymous reviewers for their constructive suggestions and comments. This work was supported by the National Science Foundation under Contract OCE-9453499, the Naval Research Laboratory under Contract NAS13-564 through the Mississippi Research Consortium and the University of Southern Mississippi, and the Office of Naval Research under Contract ONR-N0001496WX30445 (NRL Job Order 7075-06). W. T. Liu is supported by the NASA Physical Oceanography Program and NASA Scatterometer Project.

APPENDIX A

The Proof for the Joint Probability Density Function (23)

The joint PDF (23) was derived from the one-dimensional PDF (21). For convenience, we will derive (21) from (23).

The joint PDF of slopes, expressed by (23), is

$$f_{\varepsilon,\eta}(x, y) = \frac{n}{2\pi(n-1)\sigma^2}\left[1 + \frac{x^2 + y^2}{(n-1)\sigma^2}\right]^{-(n+2)/2}, \quad \text{(A1)}$$

where ε, η are the slope components in upwind and crosswind directions, respectively; x, y are the corresponding values.

Now, if

$$r^2 = x^2 + y^2$$
$$q = x, \quad \text{(A2)}$$

then from the Jacobian

$$J(x, y) = \begin{vmatrix} \frac{\partial r}{\partial x} & \frac{\partial r}{\partial y} \\ \frac{\partial q}{\partial x} & \frac{\partial q}{\partial y} \end{vmatrix}$$

we have

$$J_{(1)}(x, y) = \frac{\sqrt{r^2 - q^2}}{r}$$
$$J_{(2)}(x, y) = -\frac{\sqrt{r^2 - q^2}}{r}.$$

Using a theorem of probability theory (Ross 1993, 55–56), we see that

$$f_{R,Q}(r, q) = \sum_{i=1}^{2} f\,(x_{(i)}(r, q), y_{(i)}(r, q))\,|J_{(i)}|^{-1}$$
$$= \frac{n}{\pi(n-1)\sigma^2}\left[1 + \frac{r^2}{(n-1)\sigma^2}\right]^{-(n+2)/2} \frac{r}{\sqrt{r^2 - q^2}}, \quad \text{(A3)}$$

where R and Q are the random variables corresponding to r and q; r and q are the values of these two variables, respectively.

The probability density function of r can be obtained from (A3) as

$$f_R(r) = \int_{-\infty}^{\infty} f_{R,Q}(r, q)\, dq$$
$$= \frac{n}{n-1}\frac{r}{\sigma^2}\left[1 + \frac{r^2}{(n-1)\sigma^2}\right]^{-(n+2)/2} \int_{-r}^{r} \frac{dq}{\sqrt{r^2 - q^2}}$$
$$= \frac{n}{n-1}\frac{r}{\sigma^2}\left[1 + \frac{r^2}{(n-1)\sigma^2}\right]^{-(n+2)/2}. \quad \text{(A4)}$$

The result (A4) is just the probability density function (21).

APPENDIX B

Mean-Square Slopes

The mean-square slope, calculated from the JONSWAP spectrum (Hasselmann et al. 1973), is

$$\sigma_g^2(K, U_{10}) = [0.0033 + 0.0088 \ln(U_{10})] + 0.00219\left[\ln\frac{K^2}{K^2 + 100^2} - \ln\frac{(6\pi)^2}{(6\pi)^2 + 100^2}\right], \quad \text{(B1)}$$

where K is the wavenumber. The ratio between crosswind component and upwind component is 0.9.

The mean-square slope, calculated from the spectrum of Liu and Yan (1995), is

$$\sigma_w^2(K, U_{10}) = 0.000013\left[U_{10}^{2.1} - \left(\frac{250}{K}\right)^2\right]H \times \left[U_{10}^{2.1} - \left(\frac{250}{K}\right)^2\right]\ln\left(\frac{K^{2.7}}{4000} + \frac{U_{10}}{5}\right), \quad \text{(B2)}$$

where the Heaviside function $H(x) = 1$, when $x > 0$, and $H(x) = 0$, when $x < 0$. The ratio between crosswind component and upwind component is 0.5.

The mean-square slope detectable with optical sensor should be calculated from (B1) and (B2) under $K = 1250$ m s^{-1} because the contribution of water waves with wavenumbers larger than 1250 m s^{-1} is found to be negligible (Liu and Yan 1995; Hwang et al. 1996). The mean-square

slopes filtered by *ERS-1* C-band radar should be calculated from (B1) and (B2) when $K = 111$ rad m^{-1}. The mean-square slopes of the underlying long gravity waves can be calculated from the above formulas when $K = 6\pi$ rad m^{-1}. The detailed formula is given by Liu (1996).

The effects of wind and long dominant waves on short waves have been included in the gravity–capillary wave model of Liu and Yan (1995). Therefore, (B2) includes both the contribution of the wind-induced short waves and the modulation of long dominant waves.

APPENDIX C

Radar Backscatter Predicted by Using Different PDFs

The differences among the three PDFs of surface slopes will be examined by comparing their effects on radar backscatter in the incidence angles away from normal incidence. The three PDFs are 1) the proposed PDF (35) with $n = 5$, 2) the Gram Charlier distribution (30) (Cox and Munk 1954a,b) with the mean value of peakedness coefficients (32) and the mean value of the skewness coefficients (31), and 3) the Gaussian distribution.

Figure C1 gives a comparison of the radar backscatter cross sections (RBCS in dB), calculated from the radar backscatter theory by using the above three PDFs of ocean surface slopes, with the empirical models CMOD3 and CMOD4 in the upwind direction. Figure C2 is the same as Fig. C1, but in the crosswind direction. Figure C3 gives the results in the downwind direction. These figures show that both the Gaussian distribution and the Gram Charlier distribution fail to predict the radar backscatter. The Gaussian distribution can only describe the ocean surface slopes with very narrow spectrum. The Gram Charlier distribution can be successfully used to describe the probability density in the range of small slopes, less than 2.5 times the root of mean-square slopes, as indicated by Cox and Munk (1954a,b), but it does not work in the range of large slopes. The proposed PDF by this paper fits the Gram Charlier distribution, observed by Cox and Munk (1954a,b), very well in the range of small slopes. Its prediction of radar backscatter in the range of large incidence angles is also in a good agreement with the empirical models of *ERS-1* scatterometer wind recovery algorithms. The radar beam from large incidence angles is reflected by the tangent-planes of large slopes. Thus, the proposed PDF can be used to describe the probability density of ocean surface slopes over the full range of slopes. This is an improvement over both the Gaussian distribution and the Gram Charlier distribution.

As shown in our figures, the proposed PDF can be used successfully in the specular reflection model (Barrick 1968) to predict the radar backscatter cross sections (RBCS) in the range of incidence angles away from normal incidence. Different sea conditions demonstrate

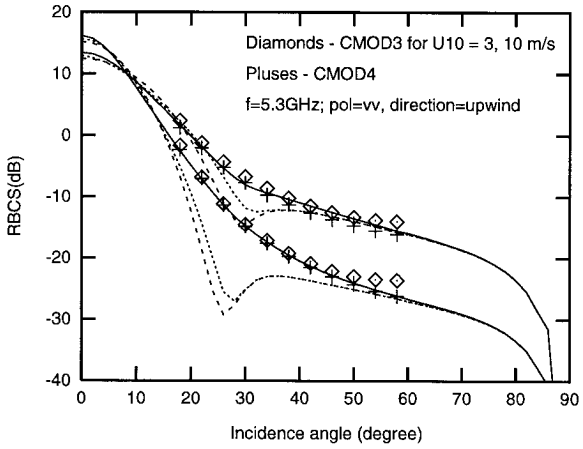

FIG. C1. A comparison of the radar backscatter cross sections (RBCS in dB), calculated from radar backscatter theory by using the three PDFs of ocean surface slopes, with the empirical models CMOD3 and CMOD4 in the upwind direction. The solid lines represent the RBCS calculated from the proposed PDF, the dashed lines represent the RBCS calculated from the Gaussian distribution, and the dotted lines represent the RBCS calculated from the Gram Charlier distribution.

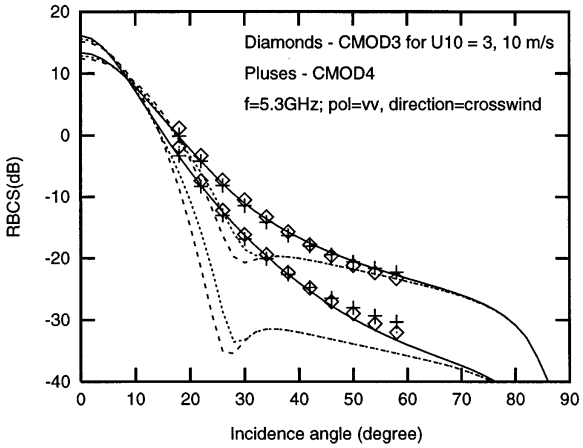

FIG. C2. As in Fig. C1 but in the crosswind direction.

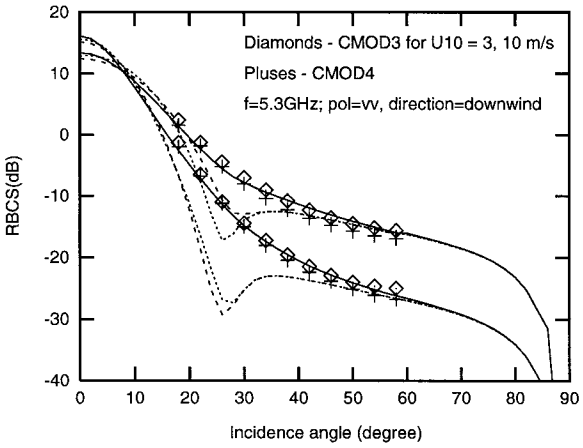

FIG. C3. As in Fig. C1 but in the downwind direction.

different spectral widths, different mean-square slopes, and different PDF of slopes, hence produce different RBCS. This is a possible explanation why there is such large scatter in the raw data obtained under low incidence angles.

REFERENCES

Abramowitz, M., and I. A. Stegun, 1972: *Handbook of Mathematical Functions with Formulas, Graphs, and Mathematical Tables.* U.S. Govt. Printing Office, 1046 pp.

Anderson, D., A. Hollingsworth, S. Uppala, and P. Woiceshyn, 1991a: A study of the use of scatterometer data in the European Centre for Medium-Range Weather Forecasts operational analysis-forecast model, 1. Quality assurance and validation. *J. Geophys. Res.*, **96,** 2619–2634.

——, ——, ——, and ——, 1991b: A study of the use of scatterometer data in the European Centre for Medium-Range Weather Forecasts operational analysis-forecast model, 2. Data impact. *J. Geophys. Res.*, **96,** 2635–2647.

Apel, J. R., 1987: *Principles of Ocean Physics.* Academic, 634 pp.

Barrick, D. E., 1968: Rough surface scattering based on the specular point theory. *IEEE Trans. Antennas Propag.*, **AP-16,** 449–454.

——, 1974: Wind dependence of quasi-specular microwave sea scatter. *IEEE Trans. Antennas Propag.*, **AP-22,** 135–136.

Bretschneider, C. L., 1959: Wave variability and wave spectra for wind-generated gravity waves. U.S. Army Corps of Engineer Beach Erosion Board Tech. Memo. 113, 192 pp. [Available from Maury Oceanographic Library, Stennis Space Center, MS 39522-5001.]

——, 1963: A one-dimensional gravity wave spectrum. *Ocean Wave Spectra*, Prentice Hall, 41–56.

Brown, G. S., 1990: Quasi-specular scattering from the air–sea interface. *Surface Waves and Fluxes*, Vol. II, G. L. Geernaert and W. J. Plant, Eds., Kluwer Academic, 1–39.

Chakrabarti, S. K., and R. P. Cooley, 1977: Statistical distribution of periods and heights of ocean waves. *J. Geophys. Res.*, **82,** 1363–1368.

Cox, C. S., and W. H. Munk, 1954a: Measurement of the roughness of the sea surface from photographs of the sun's glitter. *J. Opt. Soc. Amer.*, **44,** 838–850.

——, and ——, 1954b: Statistics of the sea surface derived from sun glitter. *J. Mar. Res.*, **13,** 198–227.

Daley, J. C., J. T. Ransone, and W. T. Davis, 1973: Radar sea return—JOSS II. Report No. 7534, 15 pp. [Available from Maury Oceanographic Library, Stennis Space Center, MS 39522-5001.]

Davidan, I. N., L. I. Lopatukhin, and V. A. Roshkov, 1973: Distributions of wave elements obtained from stero-photograph (in Russian). *Trans. State Oceanogr. Inst.*, **112,** 72–83.

Donelan, M. A., and W. J. Pierson, 1987: Radar scattering and equilibrium range in wind-generated waves with application to scatterometry. *J. Geophys. Res.*, **92,** 4971–5029.

Forristall, G. Z., 1978: On the statistical distribution of wave heights in a storm. *J. Geophys. Res.*, **83,** 2353–2358.

Gluhovskii, B. H., 1966: *Investigation on the Sea Wind Waves* (in Russian). Leningrad Press, 284 pp.

Gooda, Y., 1977: The analysis on the joint distribution of period and wave height from the records of wave observations (in Japanese). *Technol. Res. Data Estuaries*, **272,** 1–19.

Hasselmann, K., T. P. Barnett, E. Bouws, H. Carlson, D. E. Cartwright, K. Enke, J. A. Ewing, H. Gienapp, D. E. Hasselmann, P. Kruseman, A. Meerburg, P. Müller, D. J. Olbers, K. Richter, W. Sell, and H. Walden, 1973: *Measurements of Wind-Wave Growth and Swell Decay during the Joint North Sea Wave Project (JONSWAP).* Deutsches Hydrographisches Institut, Hamburg, Reihe A. No. 12, 95 pp.

Hoffman, R. N., 1993: A preliminary study of the impact of the *ERS 1* C band scatterometer wind data on the European Centre for Medium-Range Weather Forecasts global data assimilation system. *J. Geophys. Res.*, **98,** 10 233–10 244.

Huang, N. E., and S. R. Long, 1980: An experimental study of the surface elevation probability distribution and statistics of wind-generated waves. *J. Fluid Mech.*, **101,** 179–200.

Hwang, P. A., S. Atakturk, M. A. Sletten, and D. B. Trizna, 1996: A study of the wavenumber spectra of short water waves in the ocean. *J. Phys. Oceanogr.*, **26,** 1266–1285.

Jackson, F. C., W. T. Walton, D. E. Hines, B. A. Walter, and C. Y. Pend, 1992: Sea surface mean square slope from K_u-band backscatter data. *J. Geophys. Res.*, **97,** 11 411–11 427.

Jacobson, J. P., and J. M. Colonell, 1972: Spectral development of wind-generated water waves in a laboratory facility. Rep. UM-72-8, 71 pp. [Available from Maury Oceanographic Library, Stennis Space Center, MS 39522-5001.]

Kinsman, B., 1960: Surface waves at short fetches and low wind speed—A field study. Chesapeake Bay Institute Tech. Rep. 19, 581 pp.

——, 1965: *Wind Waves.* Prentice-Hall, 676 pp.

Krylov, U. M., 1956: Statistical theory and calculation of sea wind-waves. Part 1 (in Russian). *Trans. State Oceanogr. Inst.*, **33,** 5–79.

Lee, P. H. Y., J. D. Barter, K. L. Beach, C. L. Hindman, B. M. Lakw, H. Rungaldier, J. C. Shelton, A. B. Williams, R. Yee, and H. C. Yuen 1995: X band microwave backscattering from ocean waves. *J. Geophys. Res.*, **100,** 2591–2611.

Liu, P. C., and J. G. Housley, 1968: Discussion on: Laboratory simulation of sea waves. *ASCE J. Waterways Harbors Division* Amer. Soc. Civ. Eng., **94,** 529–532.

Liu, Y., 1996: The spectrum of gravity–capillary waves, the probability density function of ocean surface slopes and their effects on radar backscatter. Ph.D. dissertation, University of Delaware, 140 pp.

——, and W. J. Pierson, 1994: Comparisons of scatterometer models for the AMI on *ERS-1*: The possibility of systematic azimuth angle biases of wind speed and direction. *IEEE Trans. Geosci. Remote Sens.*, **32,** 626–635.

——, and X. H. Yan, 1995: The wind-induced wave growth rate and the spectrum of the gravity–capillary waves. *J. Phys. Oceanogr.*, **25,** 3196–3218.

Longuet-Higgins, M. S., 1963: The generation of capillary gravity waves by steep gravity waves. *J. Fluid Mech.*, **16,** 138–159.

——, 1975: On the joint distribution of the periods and amplitudes of sea waves. *J. Geophys. Res.*, **80,** 2688–2694.

——, 1982: On the skewness of sea-surface slopes. *J. Phys. Oceanogr.*, **12,** 1283–1291.

Phillips, O. M., 1977: *The Dynamics of the Upper Ocean.* 2d ed. Cambridge University Press, 336 pp.

——, 1988: Remote sensing of the sea surface. *Annu. Rev. Fluid Mech.*, **20,** 89–109.

Pierson, W. J., and L. Moscowitz, 1964: A proposed spectral form for fully developed wind seas based on the similarity theory of S. A. Kitaigorodskii. *J. Geophys. Res.*, **69,** 5181–5190.

Ross, S. M., 1993: *Introduction to Probability Models.* 5th ed. Academic Press, 556 pp.

Schanda, E., Ed., 1976: *Remote Sensing for Environmental Sciences.* Springer-Verlag, 367 pp.

Stewart, R. H., 1985: *Methods of Satellite Oceanography.* University of California Press, 360 pp.

Trizna, D. B., J. P. Hansen, P. A. Hwang, and J. Wu, 1993: Ultra-wideband radar studies of steep crested waves with scanning laser measurements of wave slope profiles. *Dyn. Atmos. Oceans*, **20,** 33–53.

Valenzuela, G. R., 1978: Theories for the interaction of electromagnetic and ocean wave—A review. *Bound.-Layer Meteor.*, **13,** 61–85.

Wen, S., and Z. Yu, 1984: *Wave Theory and Calculation Principle* (in Chinese). Science Press, 662 pp.

Wetzel, L. B., 1993: A time domain model for sea scatter. *Radio Sci.*, **28,** 139–150.

Wright, J. W., 1968: A new model for sea clutter. *IEEE Trans. Antennas Propag.*, **AP-16,** 217–223.